

Mechanism of the Asymmetric Monsoon Transition as Simulated in an AGCM

Zhuo Wang

Department of Meteorology, Naval Postgraduate School, Monterey, California

C.-P. Chang

Department of Meteorology, Naval Postgraduate School, Monterey, California

***Corresponding author address:* Dr. Zhuo Wang, Department of Meteorology, Naval
Postgraduate School, Monterey, California, 93943**

E-mail: zwang@nps.edu

Abstract

Atmospheric general circulation model (AGCM) simulations are carried out to test a hypothesis (Chang et al. 2005) for the asymmetric monsoon transition in which the maximum convection marches gradually from the Asian summer monsoon to the Asian winter monsoon during boreal fall but experiences a sudden transition in the reverse during boreal spring. In the control run, the AGCM is driven by the climatological mean sea-surface temperature (SST) with a realistic annual cycle, and it reproduces the observed asymmetric monsoon transition. In the sensitivity test, the model is driven by a similarly realistic SST but whose annual cycle is symmetric. The northwestward march of the maximum convection in boreal spring becomes more gradual, resulting in an overall near-symmetric pattern for the monsoon seasonal transition. The AGCM simulations confirm the hypothesis that the atmospheric mass redistribution due to the different land–ocean thermal memories leads to a seasonally different horizontal convergence field and it facilitates the southeastward monsoon march in boreal fall while hinders the northwestward monsoon march in boreal spring, contributing to the asymmetric monsoon transition.

1. Introduction

The region of Southeast Asian landmasses, which includes Indochina, the Malay Peninsula, and the Maritime Continent, is situated between the Asian (Indian) summer monsoon and the Asian winter (Australian summer) monsoon in both space and time. An asymmetry in the seasonal transition between the two monsoons has been noticed in many studies (e.g., Lau and Chan 1983; Meehl 1987; Yasunari 1991; Matsumoto and Murakami 2002; Hung and Yanai 2004; Hung et al. 2004; Chang et al. 2005). In boreal fall (September-October-November, or SON), the maximum convection moves near continuously southeastward from the South Asian summer monsoon region to the Australian summer monsoon region, roughly following the Southeast Asian land bridge. However, in boreal spring (March-April-May, or MAM), the convection centers mostly stay south of 5° N until the reversed meridional thermal gradient is sufficiently established at which time they suddenly jump northward.

Previous studies relevant to the asymmetric monsoon transition have suggested the possible effects of seasonal difference of Walker circulations (e.g., Wang 1994; Li and Philander 1996; Webster et al. 1998) and those of asymmetric equatorial basic flow or wave responses to heating (e.g., Matsumoto and Murakami 2002; Hung et al. 2004). Chang et al. (2005) examined the difference in sea level pressure (SLP) between spring and fall and proposed that the asymmetric transition is due to the atmospheric mass redistribution between land and ocean areas during the two seasons. They hypothesized that this redistribution is driven by the large thermal memory of the ocean, which causes

the annual cycle of SST to lag the temperatures over land by about one to two months. As a result, SST is warmer in local fall than in local spring, making SLP over ocean to be higher in spring than in fall and vice versa over land. They showed that this seasonal land-ocean SLP differences and the Asia-Australia geography can lead to asymmetric wind-terrain interactions and a low-level divergence asymmetry in the vicinity of Southeast Asia and the Maritime Continent (Fig. 1) which tends to promote the southward monsoon march during boreal fall but oppose the northward march during boreal spring.

In this study, we test Chang et al.'s hypothesis and explore the role of the asymmetric seasonal variation of SST in the asymmetric monsoon transition using AGCM simulations. The model and the experiment design are described in section 2. The simulation results are presented and discussed in section 3. Section 4 is a brief summary.

2. Model and experiment design

The ECHAM4.0 developed by ECMWF (Roeckner et al.1996) is used to test Chang et al.'s (2005) hypothesis. The model is based on the primitive equations, and forced by solar radiation, prescribed SST and sea ice. Annual and diurnal variations of solar radiation are included. The land surface temperature and temperature over ice and snow cover are predicted through energy budget calculations. The model can reproduce the realistic seasonal mean climate with remarkable skill (Roeckner et al. 1996), especially in the lower and mid-troposphere.

In this study, the horizontal variations of the model fields are solved in a spectral domain with a triangle truncation at 42 wave numbers (T42). The resolution of the corresponding Gaussian grid is around $2.8^\circ \times 2.8^\circ$. A hybrid sigma-pressure coordinate is used with 19 irregularly spaced levels and with the highest resolution in the planetary boundary layer.

Two sets of experiments are conducted to test the role of the asymmetric seasonal variation of SST, which is caused by the large thermal inertia of the ocean, in the asymmetric monsoon transition. In the control run (CTRL), AGCM is forced by the observed, seasonal-evolving, climatological mean SST. In the sensitivity test (SYMM), SST is adjusted to vary according to a symmetric annual cycle as below:

$$SST(i) = \begin{cases} 0.5(SST_{obv}(i) + SST_{obv}(14-i)), & \text{for } i \neq 1 \text{ or } 7 \\ SST_{obv}(i), & \text{for } i = 1, 7 \end{cases}$$

where i represents the calendar month, and the subscript *obv* denotes observed climatological value. The above equation mandates that SSTs in March, April, and May are the same as SSTs in November, October, and September, respectively, and thus the effects of the large ocean thermal memory are excluded, and the annual cycles of SST and land surface temperature are nearly in phase except over the Indian monsoon region, where the land surface temperature is warmest in May before the Indian monsoon onset (not shown). Since the observed SST maximum generally occurs in August or September due to the larger ocean thermal memory, the specified SST in the sensitivity test tends to be warmer than that observed in the local spring and cooler in the local fall.

In both sets of experiments, the model is integrated for twenty years to produce ensemble means for analysis. Long-term means from the Climate Prediction Center (CPC) Merged Analysis of Precipitation (CMAP) enhanced version (average from 1979-2000) (Xie and Arkin 1997) and NCEP/NCAR Reanalysis (NNR) data (average from 1968-1996) (Kalnay *et al.* 1996) are used to evaluate the simulated annual cycles.

3. Results

Figs. 2a and 2b show the differences of seasonal mean surface air temperature between boreal spring (March-April-May, or MAM) and boreal fall (September-October-November, or SON) from the NCEP/NCAR Reanalysis and the ECHAM control run, respectively. Since the observed sea surface temperature (SST) is specified in the control run and the surface air temperature over oceans closely follows SST, the seasonal difference of the surface air temperature simulated by the model resembles that observed over ocean. Positive temperature differences dominate over the Northern Hemisphere oceans except the Indian Ocean, and negative temperature differences dominate over the Southern Hemisphere oceans. Chang *et al* (2005) attributed this distribution to the warmer SST during the local fall due to the large ocean thermal memory. The negative temperature difference over the northern Indian Ocean is associated with the relatively cool SST in the boreal fall due to the wind-evaporation feedback during the monsoon season.

Over land, the NCEP/NCAR Reanalysis shows smaller temperature differences ($\leq 2\text{K}$) over most extratropical regions in the Northern Hemisphere,

but larger differences in the tropical monsoon regions with negative values in the Northern Hemisphere and positive values in the Southern Hemisphere. Most of these regions are characterized by a wet summer, and the cooler surface air temperature during local fall (SON for the Northern Hemisphere and MAM for the Southern Hemisphere) may result from the relatively moist and cool land surface after the wet summer.

Most of these observed features are reproduced by ECHAM in the CTRL run. A conspicuous discrepancy exists over the Eurasian continent, where positive temperature differences dominate the extratropical region and negative values are confined to the South and Southeast Asian monsoon regions. This discrepancy is at least partly due to excess snowfall in boreal winter in the model simulation (not shown), resulting in a colder spring in these regions. Another discrepancy is in the Polar Regions, where the model produces a cold bias during boreal fall.

Fig. 2c shows the seasonal differences of the surface air temperature in the symmetric SST run (SYMM). In this experiment, the spring and fall seasonal mean SSTs are the same, so the surface air temperature difference over ocean is negligible except over the Arctic. Over land, negative difference is again found in the tropical monsoon regions, particularly in South and Southeast Asia, and positive air temperature difference exists elsewhere. Similar to the control run, cold biases remain over the Polar Regions. Comparing SYMM with CTRL, the fall-spring difference in the subtropical (within 30° latitude) land areas is similar except over North Africa and the Arabian Peninsula, where SYMM shows a

relatively cool boreal fall. The seasonal difference of the land-ocean thermal contrast is much weaker in the SYMM run than in the CTRL run or the NCEP/NCAR Reanalysis. Note that solar radiation remains the same while the land surface temperature differences between the CTRL and the SYMM runs are quite different in some areas. This may be indicative of the impacts of the differential land-ocean heat capacity on the land-surface energy budget, which could be through advection, precipitation, cloud-radiation feedback or other processes.

The observed SON-minus-MAM seasonal difference of SLP is shown in Fig. 3a. As discussed by Chang et al (2005), compared to boreal spring, SLP in the Northern Hemisphere during boreal fall tends to be higher over land and lower over ocean, and the reverse is true in the Southern Hemisphere. This pattern is seen throughout most of the global domain except along the midlatitude storm tracks over oceanic areas. The SLP seasonal difference is consistent with the seasonal difference of the surface air temperature, and it suggests that air mass is transferred from the relatively warmer regions to relatively cooler regions, and contributes to higher spring and lower fall SLP over ocean. In Southeast Asia and the Maritime Continent, the seasonally different SLP patterns lead to a seasonally different horizontal convergence field (Fig. 1), that is conducive of deep convection in boreal fall but tends to suppress convection in boreal spring.

The CTRL simulation reproduces most of the observed features (Fig. 3b). Compared to boreal spring, SLP in the Northern Hemisphere during boreal fall is higher over land and lower over ocean, and the reverse is true in the Southern

Hemisphere. It should be noted that it is the land-ocean thermal contrast that determines the mass redistribution and the land-ocean SLP difference. Although the extratropical latitude Northern Hemisphere land in the CTRL run is mostly warmer in SON and cooler in MAM (Fig. 2b), the magnitude of the positive difference over land is weaker than that over ocean, so the seasonal difference of the land-ocean thermal contrast in the CTRL run retains the same polarity as that observed in the NCEP/NCAR Reanalysis, namely the land is cooler than ocean in boreal fall and vice versa. This leads to air mass redistribution from ocean to land and thus a higher (lower) SLP over land (ocean) in boreal fall.

Around Southeast Asia the gradient of the SLP difference fields provides the same kind of wind and convergence patterns as in Fig. 1, so that convection and continuous southeastward monsoon transition is more favored during boreal fall than during boreal spring. However, the SLP difference over East Asia is smaller than in that observed (Fig. 3a), which may be expected from the reduced land-sea thermal contrast in the CTRL run (Fig. 2b) as compared to the NCEP/NCAR Reanalysis (Fig. 2a).

In the SYMM run (Fig. 3c), SLP difference is generally much weaker than in the CTRL run, which is consistent with the weaker seasonal difference of SST. Over land, SLP tends to be slightly higher in local fall than in local spring in both hemispheres, suggesting that the observed tendency of higher SLP in local fall includes effects other than the differential land-sea heat capacity. These effects may be associated with seasonal differences in atmospheric circulations that are not directly forced by the thermal contrasts. A significant difference from the

CTRL run is over Southeast Asia and the western Pacific: the much weaker SLP seasonal differences in the SYMM run implies a weaker northeasterly wind in boreal fall. Another difference is over the equatorial Indian Ocean: SLP in the SYMM run tends to be lower in SON and higher in MAM.

The annual cycle of the observed monsoon rainfall over the vicinity of Southeast Asia, demonstrated by the latitude-time section averaged over 90°E-130°E, is shown in Fig. 4a. During boreal winter (DJF), maximum rainfall is located south of the equator, which is associated with the wind-terrain interaction over the Indonesian Archipelago (Chang et al. 2005). Rainfall weakens significantly in boreal spring (from 11 mm day⁻¹ to 6 mm day⁻¹), and the major rainfall belt (≥ 7 mm day⁻¹) remains south of 5° N until May when it jumps northward. The northward jump of the rainfall belt is accompanied by a remarkable increase of rainfall north of 8° N that marks the abrupt onset of the Asian summer monsoon. This jump is contrasted with the gradual southward retreat of the maximum rainfall from August (around 12°N) to December (near the equator), which gives the asymmetry of the seasonal transitions.

The seasonal march of monsoon rainfall in the CTRL run is shown in Fig. 4b. The maximum rainfall in boreal winter is located between 0-5°S, which is north of the observed location and also weaker than that observed. This is probably due to the relative coarse resolution of the AGCM (T42, about 2.8° X 2.8°), which is unable to resolve the complex terrain of the Indonesian Archipelago and the associated wind-terrain interaction. Despite the coarse resolution, the asymmetric monsoon transition is well reproduced by the model: the maximum

rainfall has an abrupt northward jump in boreal spring and a gradual southward retreat in boreal fall. Compared to observations, the model summer monsoon rainfall is stronger and more confined in the meridional direction, and the increase of the precipitation is delayed to May, which makes the monsoon onset more abrupt.

The rainfall in the SYMM run is shown in Fig. 4c. Compared to the CTRL run, the northward march of monsoon rainfall in boreal spring is more gradual with the jump less obvious. It is also interesting to note that precipitation in Southeast Asia (between 10-15N) starts to increase in early April, which makes the monsoon onset less abrupt in time. Meanwhile, a gap of monsoon rainfall appears in boreal fall, suggesting a significant decrease of precipitation during the southward monsoon withdrawal. The whole annually cycle pattern is evidently more symmetric than that shown in the CTRL run (Fig. 4b). Thus, when the effects of the large ocean thermal memory are removed, the asymmetry in the seasonal monsoon rainfall transition is much reduced. This result supports Chang et al.'s hypothesis that the ocean-land thermal memory difference and the resultant mass redistribution during the transition seasons play a key role in controlling the seasonal march of monsoon rainfall.

The contrast between the CTRL and the SYMM runs may also be seen in the annual cycle of the moisture convergence integrated from the surface to 200 hPa over 90°E-130°E (Fig. 5). The moisture convergence is mainly due to wind convergence in the lower troposphere (contours in Fig. 5). In the control run, it shows a sudden northward march and a significant increase in boreal spring, but

gradually weakens and retreats southward in boreal fall; in the symmetric SST run, the moisture convergence has a rather smooth northward march in boreal spring while it weakens significantly in early boreal fall.

The different seasonal variations of the simulated wind convergence may be explained by the surface air temperature and sea level pressure differences. Fig. 6 shows the SYMM minus CTRL differences of spring seasonal mean surface air temperature (Fig. 6a), SLP (Fig. 6b), 950 hPa wind and wind convergence (Fig. 6c) and precipitation (Fig. 6d). Compared to the control run, surface air temperature during boreal spring in the SYMM run is warmer in the north and cooler in the south, and SLP is lower in the north and higher in the south. The high SLP over China and the Tibetan Plateau may be attributed to the relatively cool surface temperature compared to the warm land in the west and the warm ocean in the east. The SLP differences favor stronger cross-equatorial flows over the Indian Ocean and stronger northeasterly flows along the East Asian coast in the SYMM run during boreal spring. As a result, the SYMM run produces more convergence in the equatorial Indian Ocean and the subtropical western North Pacific (Fig. 6c), which favors deep convection over the Maritime Continent and shifts the ITCZ northward over the western North Pacific in boreal spring (Fig. 6d)

In boreal fall (Fig. 7), the patterns are nearly opposite: warmer Indian Ocean and cooler western North Pacific cause lower SLP over the Indian Ocean and higher SLP over the western North Pacific in the SYMM run, which results in more divergence over the equatorial Indian Ocean and the subtropical western North Pacific. This divergence belt becomes a barrier to the southward retreat of

monsoon rainfall in the SYMM run (Fig. 7d), and results in the appearance of a slightly abrupt jump in the southward march of monsoon rainfall in boreal fall as seen in Fig. 4c. Over the western North Pacific, it leads to a southward shift of the ITCZ (Fig. 7d).

4. Summary and Discussion

The seasonal transition of the Asian-Australian monsoon is asymmetric, with the maximum convection following a gradual southeastward path across the equator in boreal fall but a sudden jump in the reversed march in boreal spring. Chang et al. (2005) hypothesized that this asymmetric transition can be explained by the land-ocean contrast of SLP during the two transition seasons which results from the large ocean thermal memory relative to land. In the vicinity of Southeast Asia and the Maritime Continent, the seasonal difference of the land-ocean SLP contrast leads to a zone of preferred low-level convergence in boreal fall and preferred low-level divergence in boreal spring. In this zone the seasonal march of monsoon convection is facilitated in boreal fall and hindered in boreal spring, resulting in the asymmetric transition.

In this study, AGCM (ECHAM4.0) simulations were used to test this hypothesis. In the control run, the AGCM is driven by the observed climatological-mean SST, and the model produced an asymmetric monsoon transition similar to that observed. In the symmetric SST run, SST is specified to have a symmetric annual cycle, so that the spring SST is the same as the fall SST and the effects of the large ocean thermal memory are excluded. Compared to the control run, the northward march of the monsoon rainfall during boreal

spring becomes more gradual while the southward retreat during boreal fall shows some discontinuity. The overall annual cycle is more symmetric. The change in the monsoon seasonal transition is consistent with the removal of the spring-fall SST difference that minimized the seasonal difference in SLP over both land and ocean and the seasonal preferential convergence/divergence zone around Southeast Asia and the Maritime Continent. Thus, the results support Chang et al.'s (2005) hypothesis.

The experiment design used to test the hypothesis is quite simple. Compared to the CTRL run, SST in the SYMM run is increased in local spring and reduced in local fall. This may also favor convection in boreal spring. However, given its small magnitude (less than 0.5 K) in the Southeast Asia/ Maritime Continent region, the direct impacts of the local SST increase are likely much less significant than those of the change of the land-ocean thermal contrast, whose magnitude is on the order of several degrees (Fig. 2). The equatorial cold tongue, which is strongest in boreal fall, is weakened in the SYMM run. It may have some remote impacts on the Maritime Continent precipitation via the Walker circulation, and favors convection over the land bridge in boreal spring, but we suspect that this is at most a secondary effect compared to the local land-ocean thermal contrast or SLP contrast.

Chang et al. (2005) also showed the important role of local mesoscale wind-terrain interaction in monsoon rainfall, in which the maximum monsoon rainfall is usually located on the windward side of high terrains rather than near the center of large-scale monsoon circulations. This effect is significant in producing the

seasonal preferential zone of convergence/divergence. Although the T42 resolution used in this study reasonably depicts the Asian and Australian continents, the Southeast Asian land bridge and the topography over the Maritime Continent are poorly represented (Fig. 8), and the model rainfall patterns have some quantitative differences from those observed. Regional climate model simulations are underway to investigate the effects of the complex terrain on monsoon rainfall.

Acknowledgements

We wish to thank Prof. Robert Haney for reading the manuscript, and thank the three anonymous reviewers for their valuable comments. This work was supported by the Office of Naval Research, Marine Meteorology Program.

References:

- Chang, C.-P., Z. Wang, J. McBride, and C. H. Liu, 2005: Annual cycle of Southeast Asia-Maritime Continent rainfall and the asymmetric monsoon transition. *J. Climate*, **18**, 287-301.
- Hung, C.-W. and M. Yanai, 2004: Factors contributing to the onset of the Australian summer. monsoon. *Quart. J. Roy. Meteor. Soc.*, **130**, 739–758.
- _____, X. Liu, and M. Yanai, 2004: Symmetry and asymmetry of the Asian and Australian summer. monsoons. *J. Climate*, **17**, 2413-2426.
- Kalnay, E., *et al.*, 1996: The NCEP/NCAR reanalysis project. *Bull. Amer. Meteor. Soc.*, **77**, 437-471.
- Lau, K. M. and P. H. Chan, 1983: Short-term climate variability and atmospheric teleconnections from satellite-observed outgoing longwave radiation. Part II: Lagged correlations. *J. Atmos. Sci.*, **40**, 2751-2767.
- Li, T., and S. G. H. Philander, 1996: On the annual cycle of the eastern equatorial Pacific. *J. Climate*, **9**, 2986-2998.
- Matsumoto, J., and T. Murakami, 2002: Seasonal migration of monsoons between the Northern and Southern Hemisphere as revealed from equatorially symmetric and asymmetric OLR data. *J. Meteor. Soc. Japan*, **80**, 419-437.
- Meehl, G. A., 1987: The annual cycle and interannual variability in the tropical Pacific and Indian Ocean regions. *Mon. Wea. Rev.*, **115**, 27-50.
- Roeckner, E., K. Arpe, L. Bengtsson, M. Christoph, M. Claussen, L. Dmenil, M. Esch, M. Giorgetta, U. Schlese, U. Schulzweida, 1996: The atmospheric

general circulation model ECHAM4: Model description and simulation of present-day climate, Max-Planck-Institute of Meteorology, Report 218, Hamburg, 90 pp.

Yasunari, T., 1991: The monsoon year - a new concept of the climatic year in the tropics. *Bull. Amer. Meteor. Soc.*, **72**, 1331-1338.

Wang, B., 1994: On the annual cycle in the tropical eastern and central Pacific. *J. Climate*, **7**, 1926-1942.

Xie, P., and P. A. Arkin, 1997: Global precipitation: A 17-year monthly analysis based on gauge observations, satellite estimates, and numerical model outputs. *Bull. Amer. Meteor. Soc.*, **78**, 2539–2558.

List of Figures:

Fig. 1 Differences of sea level pressure between boreal fall and boreal spring (SON minus MAM), Negative isobars are dotted and the zero line is dashed. Unit: hPa. Schematics of sea level wind differences based on the differences in the sea level pressure pattern are indicated. The elliptic-shaped area indicates preferred belt of convergence in fall and divergence in spring. (Fig. 10 of Chang et al. 2005)

Fig. 2 Seasonal differences (SON-MAM) of surface air temperature from NCEP/NCAR Reanalysis (a), ECHAM CTRL run (b) and ECHAM SYMM run. (Units: K)

Fig. 3 Same as Fig. 1, except for sea level pressure (SLP, units: hPa).

Fig. 4 Annual variations of precipitation over 90-130 E (units: mm day⁻¹) from CMAP (a), ECHAM CTRL run (b) and ECHAM SYMM run (c).

Fig. 5 Annual variations of vertically integrated moisture convergence (shading, units: g m⁻²) and 950 hPa wind divergence (contour, units: 10⁻⁶ s⁻¹) from ECHAM CTRL run (a) and ECHAM SYMM run (b). The moisture convergence is integrated from sea level pressure to 200 hPa.

Fig. 6 Difference between ECHAM CTRL run and SYMM run in boreal spring: surface air temperature (a, units: K), SLP (b, units: hPa), 950 hPa wind vector and wind divergence (bottom panels, shading, units: 10⁻⁶ s⁻¹) and precipitation (d, units: mm day⁻¹).

Fig. 7 Same as Fig. 6, except for boreal fall.

Fig. 8 Topography (dark shading with multiple levels; units: meters) in the ECHAM model for T42-truncation.

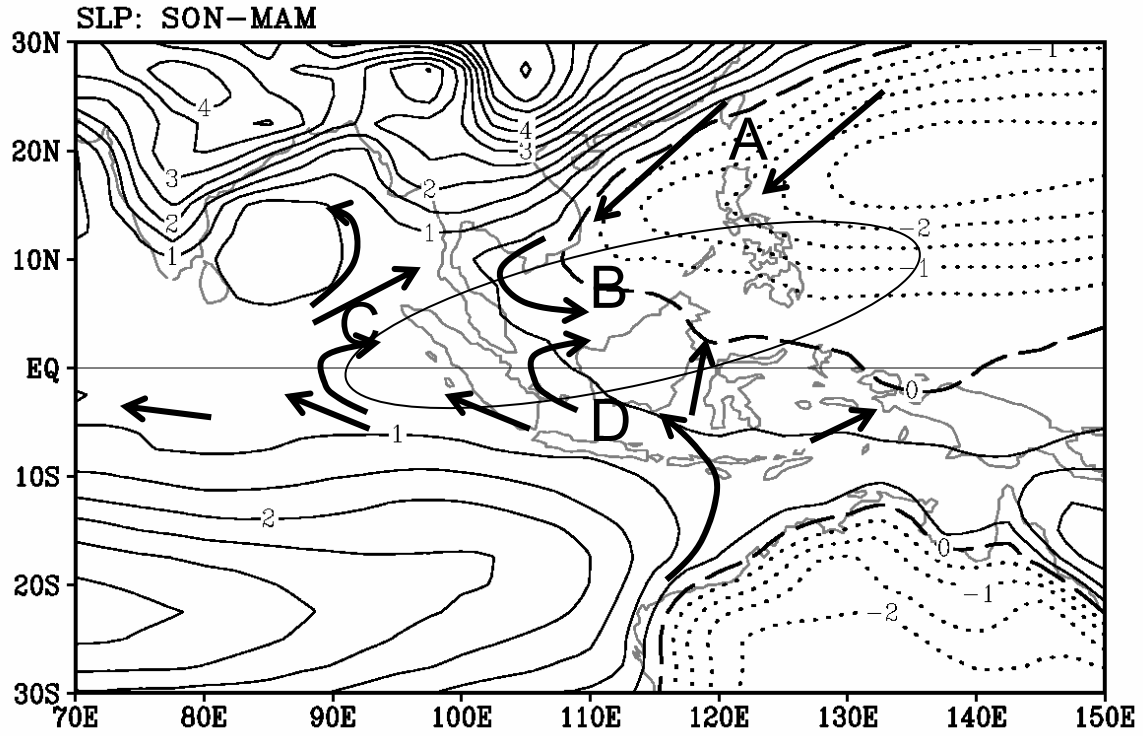


Fig. 1 Differences of sea level pressure between boreal fall and boreal spring (SON minus MAM), Negative isobars are dotted and the zero line is dashed. Unit: hPa. Schematics of sea level wind differences based on the differences in the sea level pressure pattern are indicated. The elliptic-shaped area indicates preferred belt of convergence in fall and divergence in spring. (Fig. 10 of Chang et al. 2005).

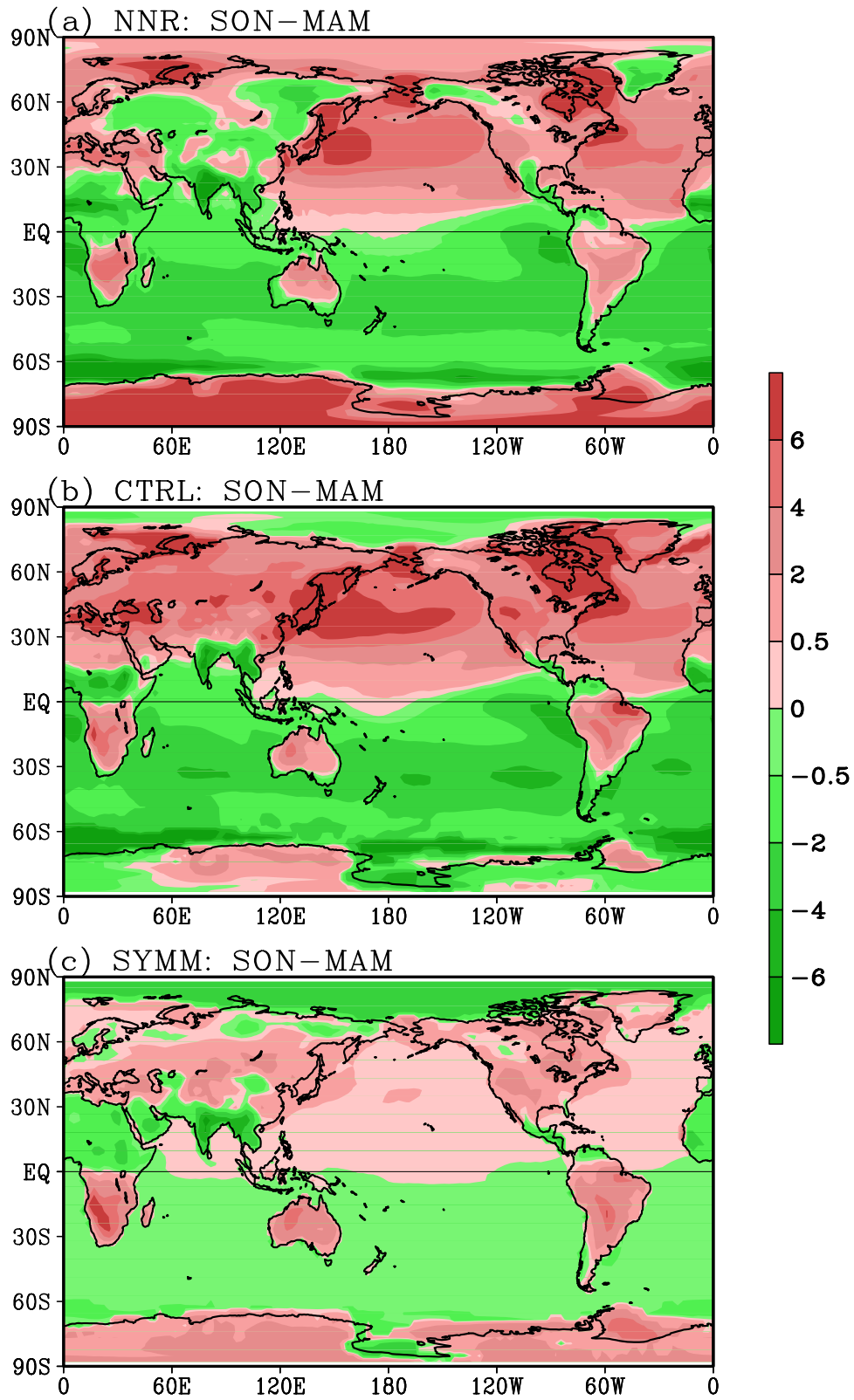


Fig. 2 Seasonal differences (SON-MAM) of surface air temperature from NCEP/NCAR Reanalysis (a), ECHAM CTRL run (b) and ECHAM SYMM run. (Units: K)

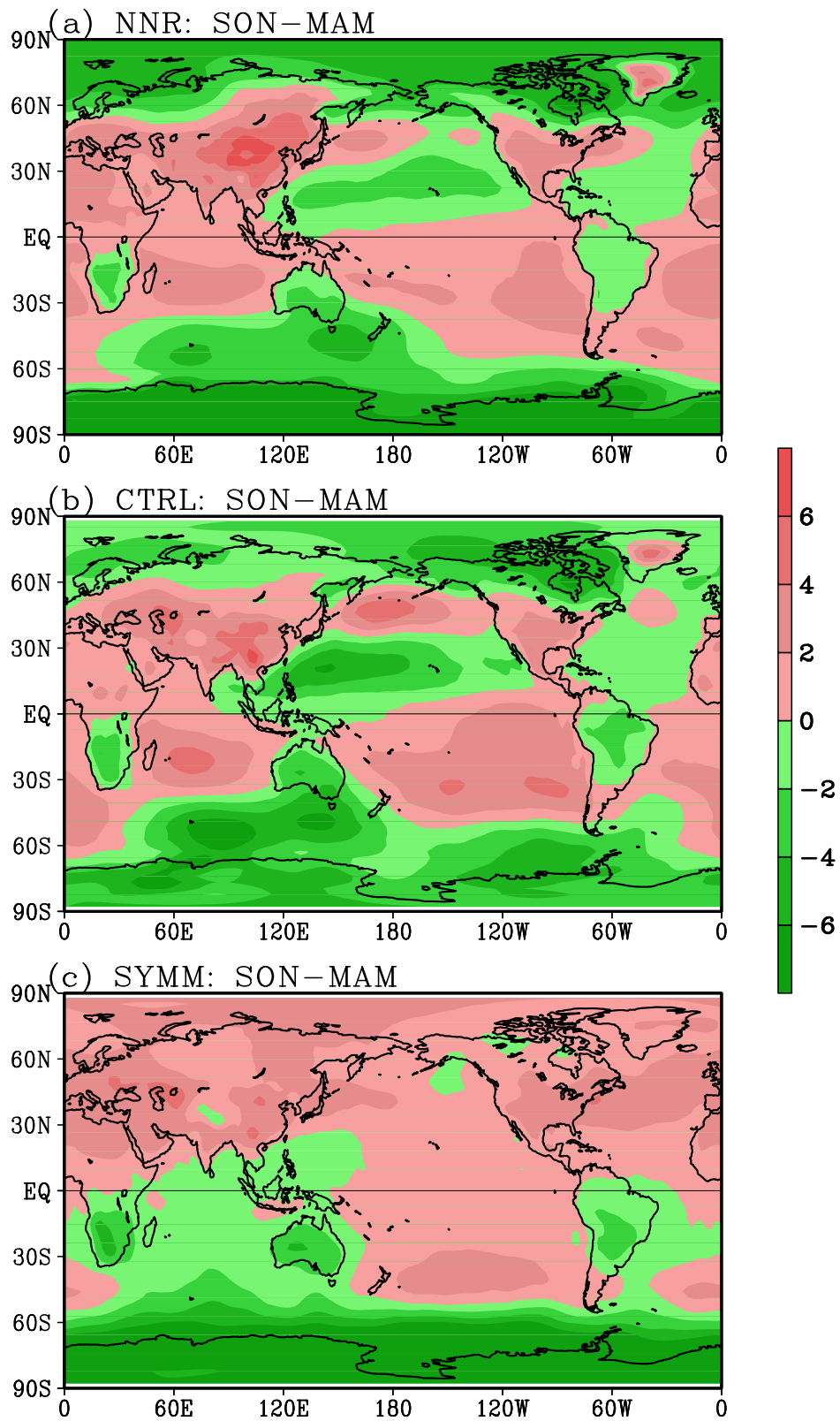


Fig. 3 Same as Fig. 1, except for sea level pressure (SLP, units: hPa).

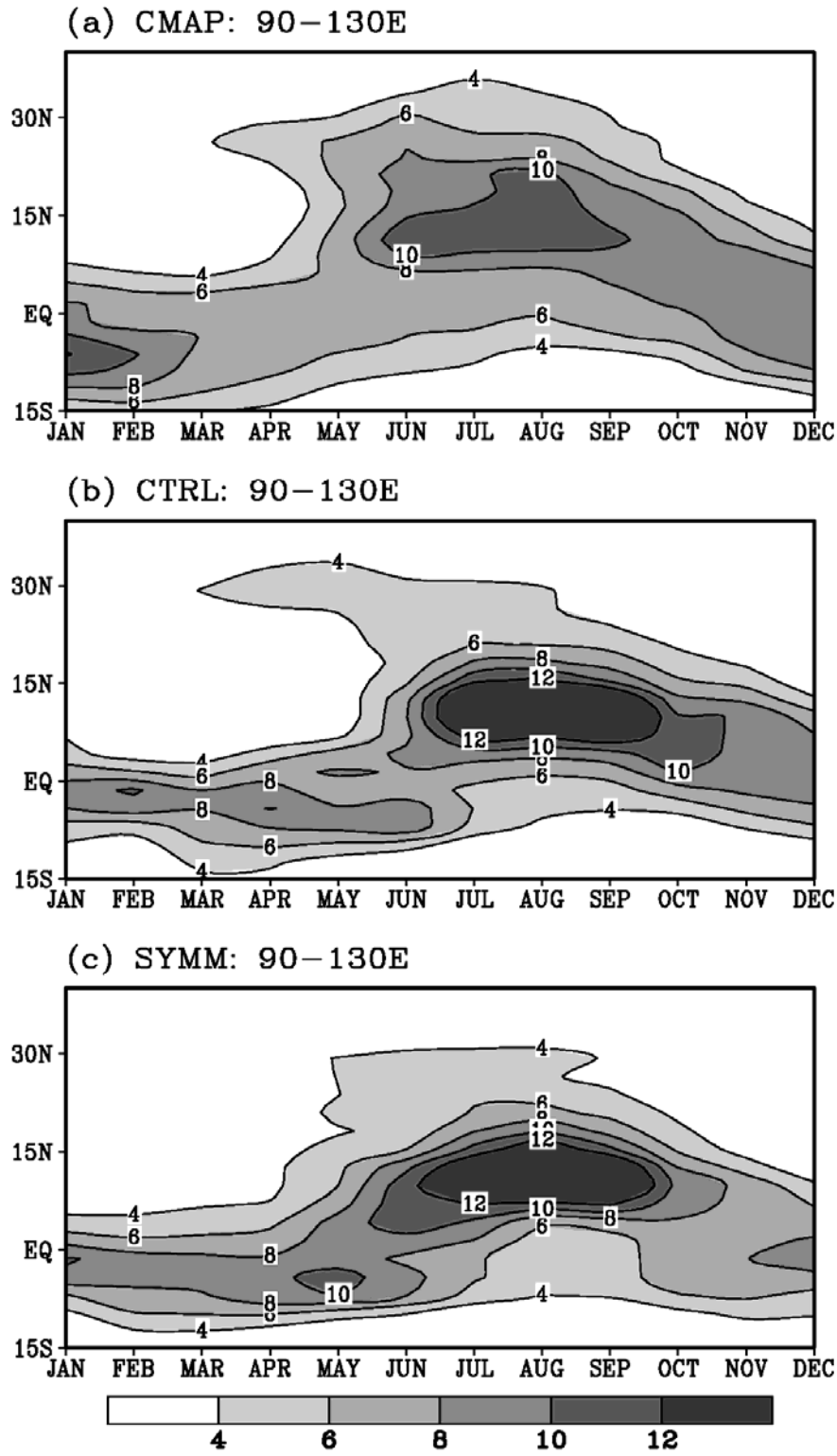


Fig. 4 Annual variations of precipitation over 90-130 E (units: mm day⁻¹) from CMAP (a), ECHAM CTRL run (b) and ECHAM SYMM run (c).

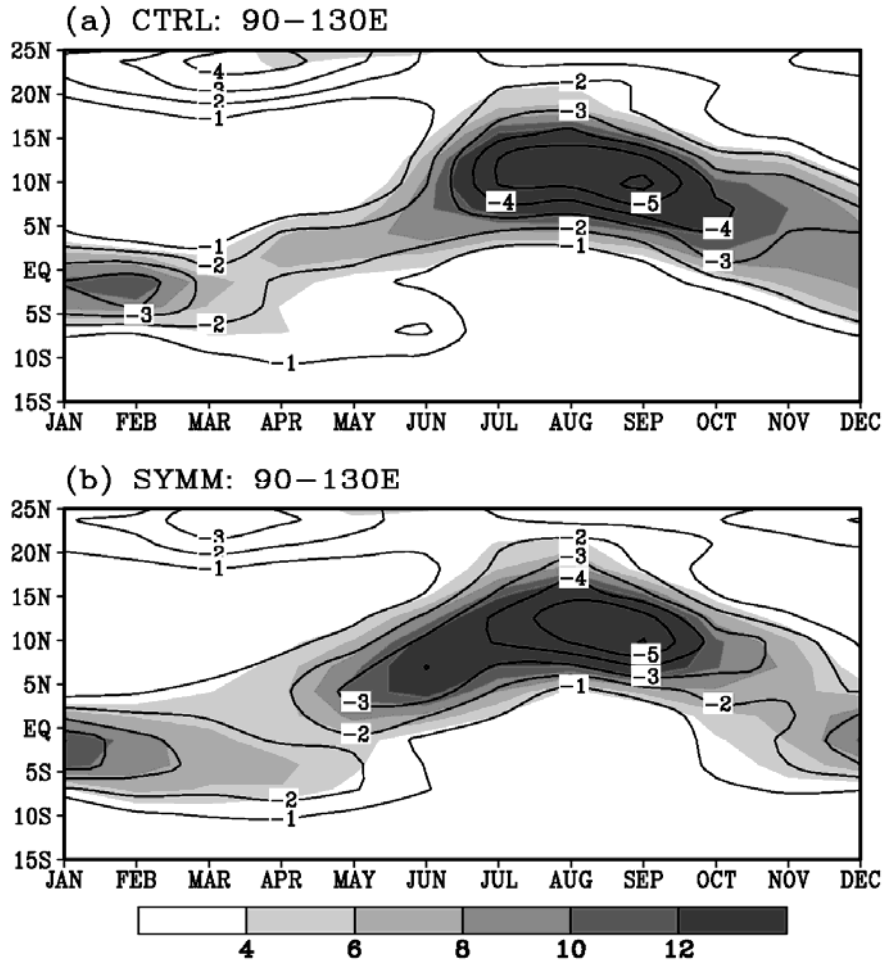


Fig. 5 Annual variations of vertically integrated moisture convergence (shading, units: g m^{-2}) and 950 hpa wind divergence (contour, units: 10^{-6} s^{-1}) from ECHAM CTRL run (a) and ECHAM SYMM run (b). The moisture convergence is integrated from sea level pressure to 200 hPa.

SYMM-CTRL (MAM)

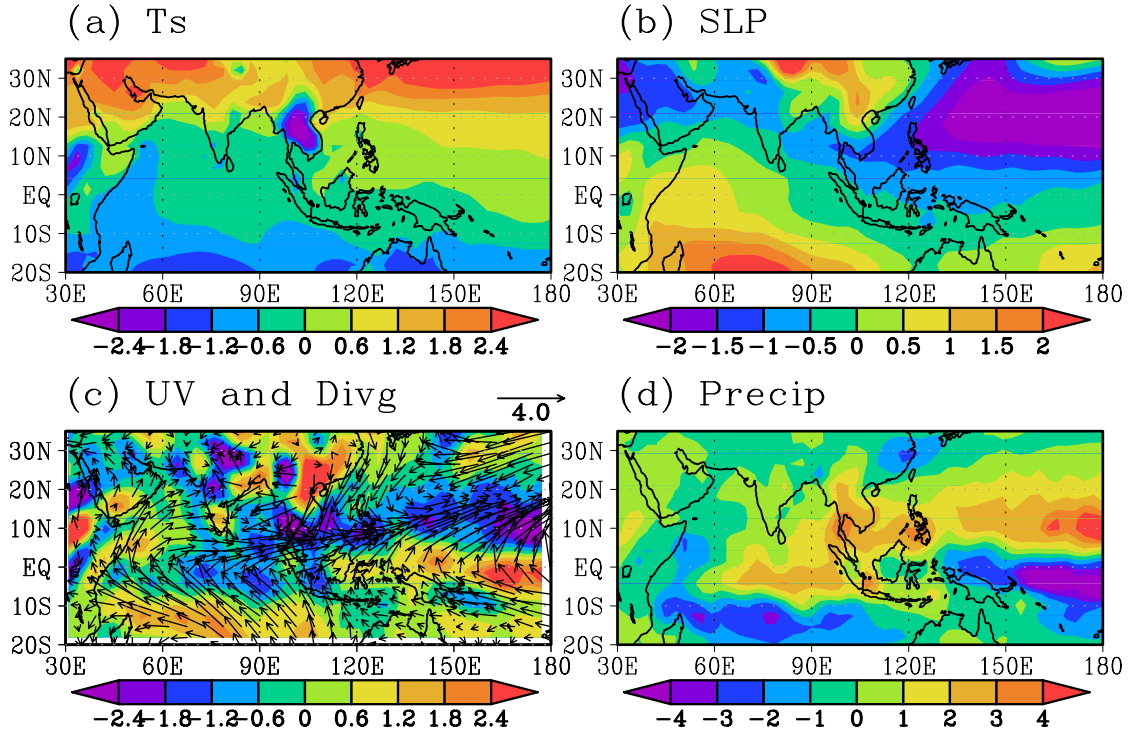


Fig. 6 Difference between ECHAM CTRL run and SYMM run in boreal spring: surface air temperature (a, units: K), SLP (b, units: hPa), 950 hPa wind vector and wind divergence (bottom panels, shading, units: 10^{-6} s^{-1}) and precipitation (d, units: mm day^{-1}).

SYMM-CTRL (SON)

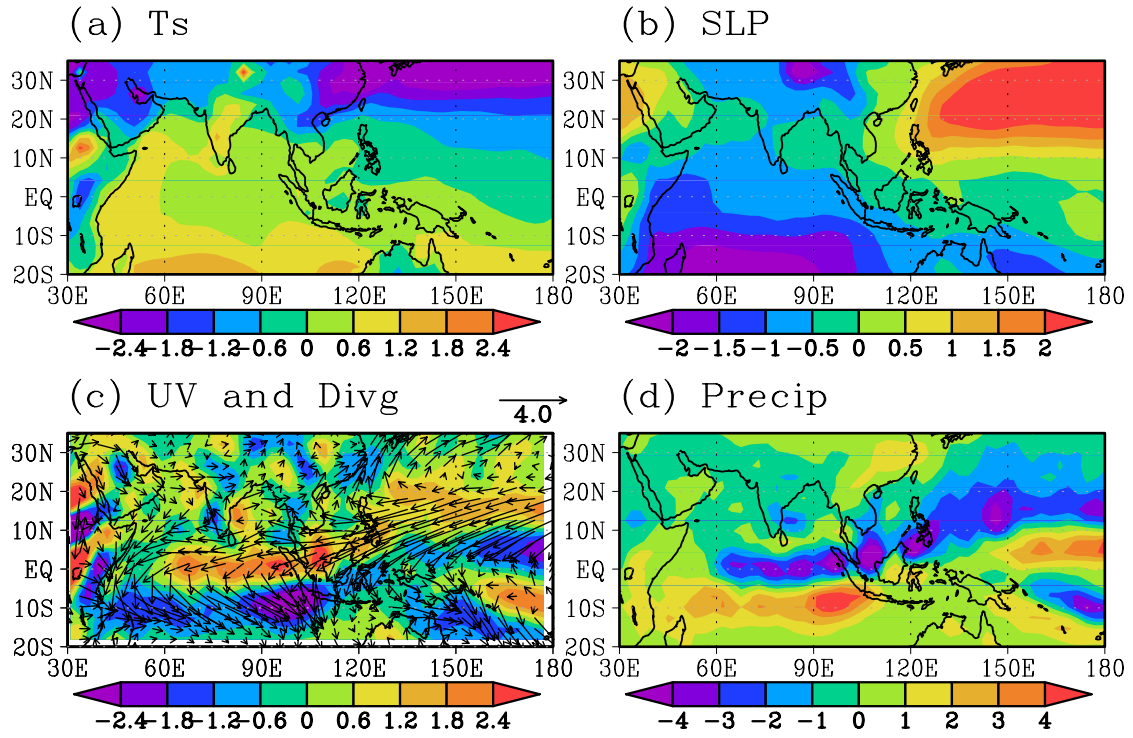


Fig. 7 Same as Fig. 6, except for boreal fall.

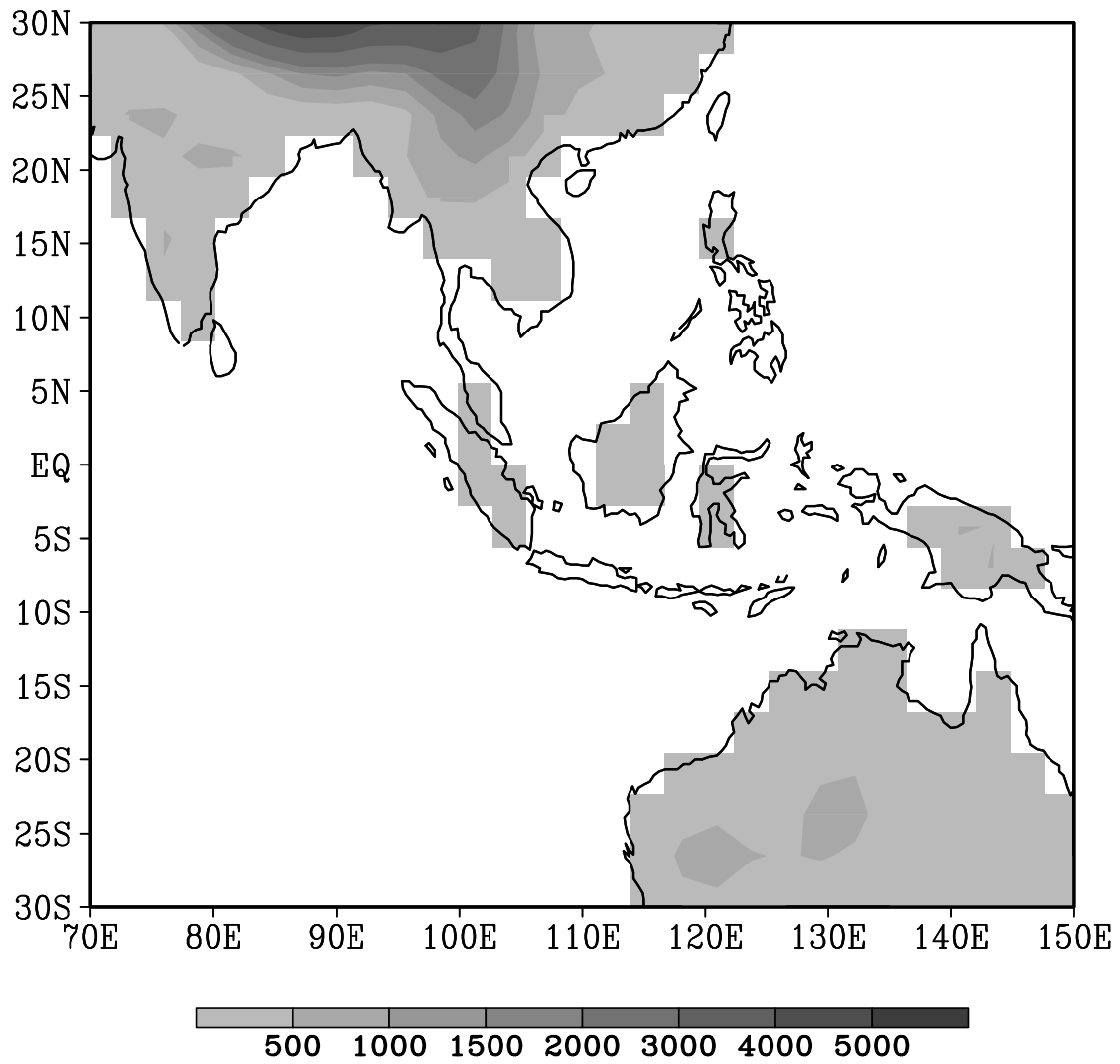


Fig. 8 Topography (dark shading with multiple levels; units: meters) in the ECHAM model for T42-truncation.